The Cryosphere Discuss., 7, 3969–4014, 2013
www.the-cryosphere-discuss.net/7/3969/2013/
doi:10.5194/tcd-7-3969-2013

The Cryosphere Discussions
Open Access

Two independent methods for mapping the grounding line of an outlet glacier – example from the Astrolabe Glacier, Terre Adélie, Antarctica

E. Le Meur[1,2], M. Sacchettini[1,2], S. Garambois[3], E. Berthier[4], A. S. Drouet[1,2], G. Durand[1,2], D. Young[5], J. S. Greenbaum[5], D. D. Blankenship[5], J. W. Holt[5], E. Rignot[6,7], J. Mouginot[6], Y. Gim[7], D. Kirchner[8], B. de Fleurian[1,2], O. Gagliardini[1,2,9], and F. Gillet-Chaulet[1,2]

[1]CNRS, LGGE, UMR5183, 38041 Grenoble, France
[2]Univ. Grenoble Alpes, LGGE, UMR5183, 38041 Grenoble, France
[3]ISTerre, UJF-Grenoble, CNRS, Saint Martin d'Hères, France
[4]LEGOS, CNRS, Université de Toulouse, Toulouse, France
[5]Institute for Geophysics, University of Texas, Texas, USA
[6]Earth System Science, University of California, Irvine, California, USA
[7]Jet Propulsion Laboratory, California, Institute of Technology, Pasadena, California, USA
[8]University of Iowa, Dept. of Physics and Astronomy, Iowa city, IA , USA
[9]Institut Universitaire de France, Paris, France

Received: 24 June 2013 – Accepted: 15 July 2013 – Published: 8 August 2013

Correspondence to: E. Le Meur (lemeur@lgge.obs.ujf-grenoble.fr)

Published by Copernicus Publications on behalf of the European Geosciences Union.

Abstract

The grounding line is a key element acting on the dynamics of coastal outlet glaciers. Knowing its position accurately is fundamental for both modelling the glacier dynamics and establishing a benchmark to which one can later refer in case of change. Here we map the grounding line of the Astrolabe Glacier in East Antarctica (66°41′ S; 140°05′ E), using hydrostatic and tidal methods. The first method is based on new surface and ice thickness data from which the line of buoyant flotation is found. We compare this hydrostatic map with kinematic GPS measurements of the tidal response of the ice surface. By detecting the transitions where the ice starts to move vertically in response to the tidal forcing we find control points for the grounding line position along GPS profiles. With the help of a 2-dimensional elastic plate model, rigid elastic deviations are computed and applied to these control points. Once the extent of the grounding zone, the kinematic approach is consistent with the hydrostatic map. These two approaches lead us to propose a grounding line for the Astrolabe Glacier that significantly deviates from those obtained so far from satellite imagery.

1 Introduction

Glaciers and ice-streams draining large ice sheets develop floating ice shelves. The transition between the inner grounded ice and its outer floating counterpart defines the so-called Grounding Line (GL). This line represents a fundamental transition in ice dynamics, separating two drastically different ice flow regimes, shear-dominant flow for the grounded part and a longitudinal stress-dominant one for the floating shelf (see for instance Pattyn et al., 2006). Proper demarcation of the GL is required for determining appropriate model discretization and mechanical equations (Durand et al., 2009; Schoof, 2007).

A second issue is that the contribution of continental ice sheets to sea level is determined by when ice passes through the grounding line and becomes afloat. As a

TCD
7, 3969–4014, 2013

consequence, any ice flow budget over outlet glaciers requires proper knowledge of ice thickness at the *exact* location of the GL. Measuring ice flux downstream of the GL can be misleading as mass exchange (mainly ice melting) takes place between the floating ice and the ocean (see for instance Gagliardini et al., 2010; Rignot and Jacobs, 2002; Joughin and Padman, 2003). Given the availability of ice surface velocities over floating ice (Rignot et al., 2011; Joughin et al., 1998) and a low vertical velocity gradient due to no basal drag on the floating ice, accurate computations of the ice flux to the ocean are now becoming possible (Shepherd et al., 2012).

In this paper we carefully evaluate methods for locating the grounding line using Astrolabe Glacier in East Antarctica's Terre Adélie as a test case. Astrolabe Glacier lies immediately next to the French Dumont d'Urville Station (see location on Fig. 1), and thus has been uniquely accessible for a range of geophysical investigations. Using a diverse range of ground, airborne and spaceborne methods, we constrain at high resolution the grounding line of Astrolable Glacier using hydrostatic and tidal methods.

2 Methods for locating the grounding line

There has been numerous large-scale attempts for delineating the GL around Antarctica using various ground, air or spaceborne techniques. The identification of the GL is complicated by the finite elastic properties of ice, which spreads the surface expression of the GL out into a wider Grounding Zone (GZ). The GZ feature most widely mapped is I_b (see Fig. 2 adapted from that of Brunt et al., 2010), a characteristic slope break thought to represent change from basal drag to no basal drag; however, additional features of the GZ relating to ocean dynamics and buoyancy provide a more direct measure of the ice-rock separation.

Buoyancy considers the ice slab in its long-term interaction with the ocean under the form of a viscous deformation when the ice comes to floatation. As the result of an essentially viscous response, no rigid stress transmission have to be considered allowing for the use of the hydrostatic approach. Effects of the tides on top of this average

TCD
7, 3969–4014, 2013

configuration can be neglected in this first computation, as they consist of limited shifts of the GL because of both the steepness of the bedrock and the limited tidal amplitude. However, tidally-induced changes in the ice upper surface can be recorded to provide a dynamical proxy for the GL under the form of respectively grounded and floating areas. Over the shorter-term forcing of the tides (5×10^{-5} Hz) the ice mostly behaves elastically (Vaughan, 1995), which leads to a regional flexure of the plate (see Fig. 3). The GZ lies between the landward and the seaward limits of this flexure (F and H, respectively, Fricker and Padman, 2006) and contains the point of separation between the ice and the bed (G, the true GL) (Fig. 2). Between F and H, the GZ is a strip whose width can be highly variable from one glacier to another, and where deviation from full hydrostatic equilibrium mainly results from the short-term tidal elastic rigid bending of the ice slab.

The difference between F and GL is not always clear, as between these two points the ice surface will undergo vertical changes whilst still being in contact with the bedrock (Figs. 2, 3 and Fig. 1 of Rignot et al., 2011). An ice upper surface undergoing tidal displacements with its base still grounded can only be explained by an elastic vertical compression of the ice column. Moreover, the pattern becomes even more complex as the GL may also migrate forth and back through the tidal cycle. This migration is all the more pronounced when the bedrock topography is flat and the tidal amplitude is large. The three approaches for mapping the GL (the hydrostatic method, the tidal method, and the surface slope method) all work by identifying characteristic GZ features.

2.1 Hydrostatic methods

Hydrostatic methods use Archimedes' Principle to estimate from surface elevation data the ice thickness required for a column of ice to float; this estimate is compared to measured ice thickness data to calculate "floatation" (Robin et al., 1983; Corr et al., 2001). Where the two numbers are the same, the ice is floating. Errors in this method come from the finite time required for ice to equilibrate once coming ungrounded, and

TCD
7, 3969–4014, 2013

from errors in surface elevation, in the value of the ice-water density contrast, and in the surface elevation and ice thickness estimates.

2.2 Tidal methods

Tidal methods consist of tracking time-dependent surface elevation changes generated by the tides (Fricker and Padman, 2006; Joughin et al., 2006). Synthetic Aperture Radar Interferometry (InSAR) has been widely employed for mapping the 2-D time-dependent vertical displacement field in response to tidal forcing (Rignot, 1998). Its landward limit theoretically yields the line of F points (Brunt et al., 2010), but Rignot et al. (2011) consider that they directly map G points instead, once their measured vertical motion is above the noise level by exhibiting regularly-spaced interferometric fringes. The question remains as to how closely the tidal method maps GL. For large scale studies, mapping F or G does not make much difference since the distance between the two is estimated to between 500 m to 1 km (Rignot et al., 2011). Similarly to InSAR, ice surface elevation temporal changes have also been assessed from ICESat repeat-track altimetry at different tidal phases (see for instance Fricker and Padman, 2006; Brunt et al., 2010 and references therein), the main limitation being a discrete number of tracks that only cross the grounding line at points spaced 10 km along much of the Antarctic coast. In this paper we use point X, the point at which flexure becomes detectable, which will be offset seaward of F toward G the true GL (Fig. 3).

2.3 Surface slope methods

Surface slope methods rely on the identification of small scale surface topographic features from visible satellite imagery or a Digital Elevation Model (DEM). These features comprise flow stripe disruption, surface manifestation of basal crevasses or a break in the surface slope (l_b) all of which are inferred to appear when the ice starts to float (Brunt et al., 2010). Scambos et al. (2007) used a constrained range of sun illumination (optimized for the expression of surface slopes) in the MODIS Mosaic image of

TCD
7, 3969–4014, 2013

Antarctica allowing for the determination of the break-in-slope (l_b) to infer a grounding line location. Horgan and Anandakrishnan (2006) used a surface slope analysis from a high resolution DEM derived from ICESat data. Bindschadler et al. (2011) used a surface slope method combining optical imagery (Landsat) with sparse ICESat altimetry for mapping the seaward limit of grounded ice features which best corresponds to l_b and constitutes their Antarctic Surface Accumulation and Ice Discharge (ASAID) GL. Bindschadler et al. (2011) provided a low resolution version of H, the limit at which ice is free floating, using a tidal analysis of the sparse ICESat data.

2.4 Differences in results

Tidal and hydrostatic methods appeared to provide a more reliable determination of the GL, but are temporally and spatially limited by data availability. Surface slope methods on the other hand can use a satellite imagery data record that extends back more than thirty years, and is not limited by decorelation due to environmental effects. In particular, this paper represents the first mapping of the Astrolabe Glacier grounding line using tidal methods, as this area was a gap in the Rignot et al. (2011) tidal grounding line dataset.

Rignot et al. (2011) find that their grounding line mapping obtained from differential satellite synthetic-aperture radar interferometry can deviate from that resulting from identification of the break-in-slope by as much as several tens of km, especially on fast moving outlet glaciers. Conversely, on more stagnant and slow-moving ice tidal and surface slope methods better agree. As a tidal approach, the approach of Rignot et al. (2011) is consistent with those based on ICESat data, the main difference being a continuous mapping along the grounding line and a much lower detection noise (vertical motion measured with millimeter precision).

In the present paper, after justifying the approach, the position of the GL of Astrolabe Glacier is first obtained from new bedrock and ice surface elevation data by applying an hydrostatic criterion. A ground based tidal approach, using kinematic GPS measurements of the tidally-induced displacement pattern of the ice slab is used for inferring

TCD
7, 3969–4014, 2013

floating and grounded areas of the glacier. With the help of a 2-D elastic rigid flexure model, the resulting positions are then corrected for this elastic effect for finally providing discrete grounding line positions for comparisons with published GL locations using the surface slope criterion.

3 Hydrostatic grounding line position

Assuming an average density ρ_i for the ice column, a theoretical floatation depth P can easily be computed from the ice upper elevation above sea level h according to:

$$P = \frac{\rho_i h}{\rho_w - \rho_i} \quad (1)$$

with ρ_w a sea water density of $1028\,\mathrm{kg\,m^{-3}}$ (Craven et al., 2005). Comparison of this depth with the depth of the ice bottom obtained from radar soundings indicates whether the ice is freely floating or is grounded.

3.1 Ice upper surface

The ice upper elevation above sea level used for computing the hydrostatic profiles has been obtained from a 40 m digital elevation model (DEM) available for the entire Astrolabe Glacier. Surface heights were calculated from a pair of stereoscopic images acquired on the 14 December 2007 by the SPOT5-HRS sensor in the framework of the SPIRIT (SPOT 5 stereoscopic survey of Polar Ice: Reference Images and Topographies) IPY project (Korona et al., 2009).

We validate the vertical accuracy of the SPIRIT DEM using Release 33 ICESat-1 data acquired during laser period 3l (Zwally et al., 2005), on average 54 days before the acquisition date of the SPOT-5 stereo pair. Before comparison, ICESat-1 elevation are converted to altitude above the EGM96 geoid to match the datum of the SPIRIT

TCD
7, 3969–4014, 2013

DEM. For each ICESat footprint, the corresponding DEM elevation was extracted by bilinear interpolation.

When correlation artifacts are discarded using the correlation mask provided with the elevation dataset, the mean vertical bias is −0.3 m (standard deviation 2.9 m, $N = 2319$). For the part of the Astrolabe Glacier studied here (close and downstream of the grounding line), there are very few interpolated pixels because the glacier surface is highly crevassed (feature rich) and SPOT5 images have a good radiometric dynamic. Thus, ±3 m is used as uncertainty for the elevation of the ice surface.

3.2 Ground penetrating radar survey

Astrolabe Glacier has been the target of several recent radar campaigns with an emphasis on the coastal part of the glacier (Fig. 4). Ground Penetrating Radar (GPR) measurements were acquired along several-km long profiles with a MALÅ® ProEx GPR system connected to a 50 MHz Rough Terrain Antenna, which was towed by the operator on the ground. Measurements were acquired with a common offset of 4 m between the transmitter and the receiver antennas. The acquisition triggering, which was fixed to 5 m for all profiles, was automatically controlled using a calibrated encoder wheel and then repositioned thanks to GPS measurements, which allow deriving topography information. Data were acquired with a sampling frequency of 648 MHz over a 12.8 µs time window, and stacked 32 times.

The GPR data were processed using the Seismic Unix software (www.cwp.mines.edu/cwpcodes). The processing sequence includes time zero corrections and "dewow" zero-phase low-cut filter to remove direct continuous currents. In order to improve signal to noise ratio of late arrivals, a zero-phase band-pass filter was also applied to raw data in the [30–70 MHz] frequency range. The data were then migrated using a Stolt f-k migration algorithm with a constant velocity of 168 m µs^{-1} in order to correctly locate dipping events and to focus scattering hyperbolas. Finally, for display purposes, topographic corrections and time to depth conversions were computed using the same constant velocity.

TCD
7, 3969–4014, 2013

This classical velocity in cold ice was measured outside of the glacier with Common Mid-Point (CMP) analyses. No firn correction had to be accounted for, given the fact that the ground radar measurements were all performed on the coastal part of the glacier where accumulated snow is generally turned into ice by the summer melting events that occur there (except over the uppermost part of profile QR). As topography variations are relatively smooth compared to penetration depth, topography corrections have been computed after migration. A gain was also applied to the data to compensate spreading signal attenuation.

Surface crevasses (seen from surface morphology (Fig. 4) and radargrams (middle of Fig. 5)) can corrupt the transmitted signal. As a result, ice thickness could only be assessed over some portions of the radar lines (black lines on Fig. 4, coloured dots show ice thickness observations). For the middle of Profile IJ, the inferred ice thicknesses should be considered with caution in the central part given the extreme weakness of the reflectors. Figure 5 shows processed radargrams corresponding to profiles QR, RU and IJ (see Fig. 4 for their respective locations).

On profile QR (Fig. 5 top), the basal interface is clearly visible as a strong unique reflector along the full profile due to thin ice ranging from 100 to 200 m on the grounded right hand side of the glacier. On profile IJ (Fig. 5 bottom) and profile RU (Fig. 5 middle), the basal interface is lost along the centerline of the glacier. This data gap could be due to the penetration limit of the GPR or to a decline in bed reflectivity. Indeed, weak focused hyperbolas are visible on the right part of profile IJ that may be resulting from the rough contact arising when the ice becomes afloat (Vaughan et al., 2012). This roughness in the basal interface could be due to salt water intrusions into bottom crevasses and cracks that creates large scattering hyperbolas that are not visible at the ice/bedrock interface (Van der Veen, 1998). For profile RU, the loss of signal in the central part is abrupt and occurs at different depths, 200 m on the left and 500 m on the right despite post-processing attempts to improve the signal to noise ratio.

TCD
7, 3969–4014, 2013

3.3 Hydrostatic profiles

From the upper ice elevation along radar profiles where the ice bottom reflector can be unambiguously identified (coloured dots on Fig. 4), Eq. (1) is used to compute the corresponding theoretical profiles of floatation depths. A density of 1028 kg m^{-3} is commonly accepted for sea water (Craven et al., 2005). Ice density is less well constrained. Various studies dealing with Antarctic ice shelves (Fricker et al., 2001; Wen et al., 2007, 2010) suggest a column-integrated ice density ranging from 880 to 900 kg m^{-3} whereas Bamber and Bentley (1994) find a good fit in the comparison of satellite altimetry and ice thickness measurements with a higher value of 917 kg m^{-3}. In our case, the presence of intense and deep crevassing in the area counteracts the lack of a firn layer which led us to adopt a value of 890 ± 10 kg m^{-3}.

Resulting profiles are depicted on Fig. 6. By denoting the bottom of the ice slab, the radar reflector is normally either above floatation (grounded ice), or lying within the floatation error bars (floating). As indicated by the error bars, floatation depth uncertainties are sensitive to the ice density range. On profile IJ the ice bottom sometimes lies below the bottom of the error bars. We believe this discrepancy is due to biases on the inferred depths of the ice bottom as (i) the excellent match of the two curves all along the T-U profile indicates that the nominal value of 890 kg m^{-3} is correct, (ii) areas where radar depths are too deep come from a poorly resolved part of the radar profile and (iii) the radar method itself as well as the interpretation of the data is subject to large uncertainties. The major uncertainty in radar data is to be found in the interpretation of radargrams where some subjectivity sometimes leads to erroneous interpretations especially with vanishing reflectors as is probably the case for the middle of profile IJ. Moreover, there is also a potential uncertainty on the depths deduced from the travel time of the electro-magnetic radar wave. Despite the lack of firn, slight deviations from this value can lead to shifts in the inferred depths.

In some cases however, radar reflectors significantly above the theoretical floatation depth are a clear indicator of grounded ice like for instance along profiles QR,

TCD
7, 3969–4014, 2013

LN, OP and RS. Conversely, a good match between profiles (for example profile T-U) most probably indicates ice which is at or near floatation. Last, along profile IJ we find grounded ice in its outer parts, which then becomes afloat (or slightly grounded) in its central part. Based on these results, we propose areas of respective grounded and potentially floating ice for the GZ of Astrolabe Glacier.

3.4 Supplementary airborne radar data

As part of a collaborative project with the Jet Propulsion Laboratory (Warm Ice Sounding Explorer, WISE) and the University of Texas (International Collaborative Exploration of the Cryosphere for Airborne Profiling, ICECAP, Young et al., 2011), several airborne geophysical campaigns have been undertaken during the 2008/2009, 2009/2010 and 2011/2012 seasons in order to characterize some of the large outlet glaciers of the Wilkes Land - Terre Adélie sector of East Antarctica. Some of the flights were dedicated to the Astrolabe Glacier over which bedrock topography was measured with a combination of medium (2.5 MHz) (MF) and very high (60 MHz) frequency (VHF) high power sounding radars mounted on either a DHC-8 Twin Otter or a DC-3T Basler aircraft. A treatment similar to that applied to ground radar data was performed and allowed for similar theoretical hydrostatic floatation profiles as those depicted on Fig. 6. A compilation of floatation results for both ground and airborne data is shown in Fig. 7. Using a density of 890 $kg\,m^{-3}$, the floating/grounded transition would be at the green to blue color change; using a density of 880 $kg\,m^{-3}$ the transition would occur between the light and darker green change (see the inset). Generally the denser the ice, the more reduced the central floating part. The high sensitivity of the floatation depths to ice density does not result here in large shifts of the floating/grounded transition simply because of the steep bedrock slopes that characterize the underneath fjord. The width of the intermediate colors along the profiles is rather short (Fig. 6, insert) meaning that changing the ice density by 10 $kg\,m^{-3}$ does not imply large lateral shifts of the floating/grounded transition.

TCD
7, 3969–4014, 2013

On the other hand, the pattern of the respective floating and grounded areas is not very clear with many blue "intrusions" within green areas and vice versa. If pinning points or troughs in the bedrock topography can not be discarded, most of these features are certainly the results of the large uncertainties in the radar depths. This is confirmed by significant thickness discrepancies at crossing point of radar lines (where for instance a light green line crosses a dark blue one without intermediate colors, see Fig. 7). Those discrepancies occur between ground and airborne lines (like over the green descending straight airborne portion that intersects the blue part of the IJ profile on the right-hand side of the glacier) but also between lines from the same airborne data set (as observable from the inset of Fig. 7).

The radar beam spot at the basal interface ranges from 1 km across for the VHF to several km for the MF system so that any rough topography in that spot can appear to map directly below the aircraft. As a consequence, a RMS of 50 m for this depth offset is common which leads to some of the observed discrepancies. As a consequence, when outlining our so-far proposed grounding line by using the central ice density value of 890 $kg\,m^{-3}$, preference was given to ground radar data when they were conflicting with airborne ones. The resulting proposed grounding line is displayed by the purple line on the figure and significantly deviates from those proposed by Bindschadler et al. (2011) and Scambos et al. (2007) especially on the left flank of the glacier.

4 Kinematic GPS grounding line position

As an independent test of GL position, we used a ground based tidal method of detecting the presence or absence of tidally-induced vertical movements of the ice upper surface using kinematic GPS positioning. Profiles of individual measurement points were set up in both along flow and cross flow direction (see green dots on Figs. 4 and 8).

TCD
7, 3969–4014, 2013

4.1 Field differential GPS survey

The method is here very similar to IceSAT repeat-track analysis (Brunt et al., 2010) as it consists of measuring the ice surface height at low and high tides and observe where the resulting 2 profiles diverge as a result of tidal movement. Tidal amplitude in the sector is ∼ 1 m (see Fig. 9). As ice shelf vertical displacements are damped by the rigid behaviour of the ice slab confined within a narrow embayment, the method requires a high accuracy in the measurements of the resulting limited vertical displacements of the ice surface. We here used carrier-phase differential GPS measurements as in Vaughan (1995). A reference GPS receiver was set up on the nearest rock outcrop, while a rover unit was used to acquire positions according to the "Stop and Go" method over the successive points constituting the profiles (Fig. 8). The corresponding baseline was short enough (15 km at the most) so as to ensure real time radio transmission of appropriate corrective terms (mostly ionospheric and atmospheric delays) from the reference to the rover and to allow for kinematic ambiguity resolution with "stop" recording phases not exceeding 30 s. Each of the measured points was precisely marked on the ground (using paint) in order for the second measurement to be performed at exactly the same place some 12 h later. Accurate reoccupation was vital as the small-scale roughness of the glacier surface is such that moving half a meter is enough to change the surface height by as much as several tens of cm.

4.2 Time-dependent ocean tides

The planning of the GPS surveys was dictated by the need for targeting highest and lowest tides. Unfortunately, the tide gauge at the nearby Dumont d'Urville station was not operational and we therefore had to rely on a prediction model (courtesy of Benoît Legrésy, see also Legrésy et al., 2004). Fig. 9 shows the model predictions for the tides of January 2011. This model was tested through our own ocean tide measurements. Vertical displacements of the nearby sea ice have been recorded for a couple of days and compared to the model results (Fig. 10). Despite a hardly perceptible discrepancy

TCD
7, 3969–4014, 2013

in the amplitudes, the phasing is perfect which allowed us to trust the model for planning our surveys and comparing our time-dependent surface height measurements to actual tides (as in Sect. 4.2.2).

4.2.1 Scaled profiles of time-differential elevation

Ice surface elevation along profiles [AB], [CD] and [EF] (Fig. 8) was measured at both high and low tides over chosen periods during which the tidal amplitude was as pronounced as possible. Measuring an entire profile (several hundred points) could sometimes last a couple of hours. Consequently, as mentioned by Vaughan (1995), the resulting profiles could not be considered as snap shots since the tide had time to evolve during the measurement period. Profiles were then scaled to the tidal amplitude e according to Eq. (5) of Vaughan (1995):

$$d = \frac{e - e'}{p - p'} \tag{2}$$

where e, e', p, p' are surface elevation and tidal prediction at respectively high and low tides and d represents the scaled displacement.

We find that this scaling is a good indicator of the 'degree of floatation' with values close to unity (100 %) as floatation approaches full hydrostatic equilibrium.

Profile [AB] (Fig. 11, top) shows the ice surface altitude profile along flow and the elevation difference between low and high tides. This difference overcomes the noise at about 4000 m along the profile (Fig. 11, top; black vertical line). According to Sect. 1 and Fig. 3, this distance corresponds to point X somewhere between points F and G and can therefore be considered as a first approximation of GL to within 0.5 km to 1 km (hereafter called "control point"), which more or less corresponds to the usual F-G distance for such glaciers (see for instance Rignot et al., 2011). X is defined where the height difference is considered as significant above the noise level (about 10 to 15 cm depending on the GPS data quality). X's closeness to GL depends on the rigid elastic

TCD
7, 3969–4014, 2013

behaviour of the ice slab in response to the high frequency tidal loading. The resulting 5 control points are displayed along their respective profiles on Figs. 4 and 8.

The figure reveals that full free tidal movement is never reached along the profile (50 % at the most). The rigid bending of the ice slab partly explains this pattern, especially given the lateral confinement of the glacier within the narrow underneath fjord. Our hydrostatic calculations show that along this profile, ice rapidly becomes grounded again after a floatation length of less than 2 km (as visible within the red inset of Fig. 7). An inflexion in the tidal elevation range is noticeable at the distance of 7000 m and is compatible with partial grounding slightly above drop point 2 (see Fig. 8). The rapid regrowth of the tidal elevation range at the end of the profile indicates that the ice is again ungrounded. Given the respective accuracies of the floatation and tidal methods and specifically the uncertainties associated with airborne radar depths, the hydrostatic floatation GL needs to be shifted landward in order to match with the recovery of floatation at the end of the profile after local grounding at the drop off point 2.

The lateral effect is confirmed by downstream and upstream cross-profiles ([EF] and [CD], respectively) where full floatation (100 %) is not reached even above the middle of the fjord (middle of profiles in Fig. 11); however, point X can be determined from the data. Data for profile [CD] was noisy due to a poor satellite GPS constellation during one of the transects. Despite an uncertainty of at least 20 to 30 cm, a difference between high and low tide profiles is perceptible and has finite vertical displacements in the central part. Although the proposed positioning for the 2 control points remains questionable over this specific profile, the presence of an uplifted central zone is confirmed by a time-dependent tidal signal (see Sect. 4.2.2) already detectable at drop off point 3 upstream of the [CD] profile (Fig. 12).

4.2.2 Time-dependent tidal measurements

We confirm this result with continuously measured surface displacements with GPS receivers placed on the ground for several days and recording in the differential mode. Four points (from Point 1 to Point 4) were selected along the Proffile [AB] (Figs. 4, 8,

TCD
7, 3969–4014, 2013

Fig. 11, top) and corresponding surface vertical displacements displayed on Figs. 12 and 13. Point 1 is roughly situated in the middle of Profile [EF] and at the extremity of profile [AB] and shows a clear tidal signal whose amplitude is 55% of the predicted tidal range, consistent with the scaled altitude differences found on Fig. 11. There is a small shift in phase, with the shelf responding with a time lag of the order of one hour. A possible explanation for the phase offset is the propagation offset of the tidal signal from the open ocean to grounding zone through the ice shelf cavity. A small anelastic component in the ice deformation is also possible as ice exhibits a visco-elastic behaviour at tidal periods (Gudmundsson, 2011). Scaled vertical displacements reaching about 50% are incompatible with the glacier grounded at this point as given by the hydrostatic method and thus confirms the need for a landward offset of the flotation derived GL.

At point 2, a phasing is still visible but the amplitude is here reduced (about 20 to 25% of the tidal amplitude) and compatible with a slightly grounded point still undergoing surface displacements from the elastic regional bulging of the ice slab. Point 3 requires a strong vertical exaggeration to exhibit a phasing that hardly overcomes the noise level. Last, no tidal signal is detectable at point 4 which lies sufficiently far inland from the grounding line for not showing any remote effect from the elastic behaviour of the slab. This is consistent with GL lying between between points 3 and 4.

5 Elastic plate modelling

We find broad consistency in the separation of the hydrostatically derived G and the tidally derived X points, respectively. Modelling the tidally-induced elastic rigid behaviour of the ice slab is an independent way of assessing this distance and therefore deducing this degree of consistency. The elastic response of the glacier to the tidal push within the fjord is computed and corresponding results analysed in terms of (i) ice slab thickness and (ii) size of the loading pattern. The G-X distance is the result of the rigid behaviour of the plate (contrary to a local response where the two points would

TCD
7, 3969–4014, 2013

overlap). It is well known that deviation from a local hydrostatic equilibrium for a rigid slab is a function of both its flexural strength (proportional to its thickness raised at the third power) and, to a lesser degree, to the spatial extent of the load (e.g., Le Meur, 2001). In this case, the latter effect is forced by the narrowness of the fjord, which prevents the ice from exhibiting full floatation with respect to the tidal forcing (see section 4.2.1). The shape of the fjord as far as it can already be assessed from the preliminary outlining of the grounding line (as represented on Figs. 7 and 8) shows a varying width ranging from about 5 km down to 1 km or so. Last, because the 2-D model as used here can only deal with a uniform thickness, sensitivity tests are also performed with regards to the thickness of the plate.

5.1 Elastic plate theory

The 2-D elastic bending in response to a point load q of a rigid elastic plate floating over an inviscid fluid of density ρ_w is given by the following constant coefficient differential equation of Brotchie and Silvester (1969) in which the momentum due to the Earth curvature can be neglected:

$$D\nabla^4 w + \rho_w g w = q \tag{3}$$

where w is the downward deflection, ∇ the 2-D gradient operator and D the flexural rigidity of the plate given by:

$$D = \frac{E H^3}{12(1-\nu^2)} \tag{4}$$

with E the Young elastic modulus taken equal to 0.9 GPa (Vaughan, 1995) , ν the Poisson coefficient (0.3) and H the plate thickness. The term $\rho_w g w$ represents the buoyancy force resulting from the downward displacement w within the fluid. As a consequence, the water push forcing resulting from a tidal amplitude of δm can be expressed as $\rho_w g \delta$ which in the absence of surface load ($q = 0$) leads to:

$$D\nabla^4 w + \rho_w g(w + \delta) = 0 \tag{5}$$

TCD
7, 3969–4014, 2013

Solution to a point load q is a deflection profile as a function of the scaled distance $r = x/L_r$, x being the true distance and $L_r = (\frac{D}{\rho_w g})^{1/4}$ a flexing width. It reads:

$$w(r) = \frac{q}{2\pi\sqrt{D\rho_w g}} kei(r) \quad (6)$$

where q is here a '"negative" load equal to $-\rho_w g\delta$ and kei the Kelvin function of zeroth order. Since the elastic bending of a rigid plate is a linear process with respect to the load, the actual response to a realistic load reads as the sum of the contribution to all of the points that constitute the loading pattern. The plate deformation finally expresses under the form of the spatial convolution of that load distribution with the 'unit response' as given by Eq. (6).

5.2 Experimental set up

In the present simulation, the domain has been digitized on a 100 m × 100 m grid representing a 12 by 10 km rectangle over which different loading patterns are tested. The pattern of the load (water push) is here featured as a simple fjord with parallel walls and terminating under the form of a semi-circular shape whose radius is half the width between the walls. Different shapes are tested with a terminal radius ranging from 500 m to 5 km as depicted in green in the bottom part of Fig. 14 (implying fjord widths from 1 to 10 km). The figure shows the case of the elastic rigid bulging of a 800 m thick ice slab in response to a 1 m water push over the 5 km wide fjord here depicted in red.

5.3 Results in terms of deviation from hydrostatic equilibrium

We find that the surface response is not local, extending beyond the limits of the underlying water push. Deviation from a local (hydrostatically equilibrated) deformation can be assessed from the spacing between the 0-deformation contour and the outline of the load. Cross sections confimrm a clear estimation of this rigid behaviour expressed by the shift between the termination of the load (point G) and the actual point of zero

TCD
7, 3969–4014, 2013

deformation (Fig. 15). More specifically, the G-X distance is here deduced from the intersection with the 0.15 m ice surface uplift (green line) corresponding to our estimated GPS detection threshold.

We note that the chosen example with a 5 km-wide fjord more or less matches the configuration along profile IJ (Fig. 5) and agrees with partially free floating ice on the cross profile as was actually measured. However, the model gives a central displacement 75 % that of the tide whereas measurements are only 50 %. The suspected nearby pinning point close to drop off point 2 (Fig. 8, not included in the model) is likely responsible and would explains such a discrepancy. The main weakness of the proposed model comes from its inability to account for a varying thickness of the slab (whereas this latter varies from 400 m to 1000 m along the IJ profile). Rather than trying to (improperly) reproduce a given configuration, it was instead decided to span a whole range of values for both the ice thickness and the loading shape that are to be expected over the glacier so as to assess the corresponding orders of magnitude for the G-X distance.

Corresponding results are displayed on Fig. 16, where the G-X distance is depicted as a function of both the plate thickness and the semi width of the ocean forcing (curvature of the terminating fjord). The figure shows limited G-X distances when the plate thickness is small whatever the size of the load. It is simply the result of a shorter flexing width when the overall rigidity of the plate is reduced. Similar G-X distances are also found with a thicker slab if the load remains limited. In this latter case, the shortness is due to the small-sized load to which the rigid plate responds with small vertical displacements. Only large-scale loads associated with a thick ice slab lead to significant G-X distances.

5.4 Updated grounding line position

The consistency between the hydrostatic and the GPS kinematic methods can now be assessed by positioning each of the 5 GPS control points within the parameter space (size of the load/ice thickness) and estimating the corresponding G-X distance. From

TCD
7, 3969–4014, 2013

the surface heights, assuming floatation, a good estimation of the ice thickness can be derived for points A, C, D, E, F which respectively gives 1050, 950, 950, 325 and 500 m (control point being here labelled according to the kinematic GPS profiles naming as proposed in Figs. 8 and 11). As for the size of the tidal water push pattern, given the presumed shape of the underneath fjord, a semi width of 1 km can be associated to the upstream A, C and D points.

For downstream points, a fjord width of some 2 km seems relevant for Point F on the right flank of the glacier, whereas the suspected rock apron upstream of control point E probably locally reduces the curvature of the loading pattern down to about 1.5 km. The resulting parameter combinations (see their positions in Fig. 16) yield G-X distances of about 600 m for the A, C and D points, a distance of some 900 m for point F and finally a distance of 750 m for point E. Assuming the kinematic GPS data are more reliable than the radar hydrostatic ones (due to the large uncertainties associated with the static approach as described in Sect. 3.4), the so-far proposed grounding line should match our "GPS control points" once they have been shifted by about the appropriate G-X distances as computed above. The laterally offset GL from control points D and C by the suggested amounts leads to a completely grounded CD profile (even if only slightly grounded); the equivalent GL for point A lies slightly downstream of the CD profile (Fig. 18).

By assessing ice thickness and fjord width at drop-off points 1 and 2, B1-B2 cross sections at these same points have been similarly modelled and corresponding results depicted on Fig. 17. Intersection of these profiles with the corresponding percentage of floatation represented by the green horizontal line indicates where drop-off points are situated with respect to GL (here featured as the outer limit of the load). These results show that the grounding line lies some 500 m inland of point 1 and some 800 m seaward of point 2, allowing for a GL positioning consistent with our preceding control points assesment. All these data put together lead us to propose an updated grounding line position (Fig. 18).

TCD
7, 3969–4014, 2013

6 Conclusions

The methods as described here represent two independent means of mapping the grounding line of a coastal glacier like Astrolabe Glacier. Our study shows that under most conditions prevailing over such glaciers (size of the fjord, thickness of the ice) the offset between the hydrostatically equilibrated grounding line and the landward limit of the ice upper surface displacements remains limited and barely exceeds 1 km. Moreover, the GPS kinematic method maps points which are actually closer to their static counterparts because the uncertainty of the method requires a detection threshold to be overcome. Both radar and GPS measurements presented here tend to confirm this consistency. Indeed, GPS measurements once corrected according to the results of a 2-D elastic plate deformation suggest a grounding line that remains within the error bars of the hydrostatic approach that comprise uncertainties on both the ice density and the radar measurements.

Our final result is a grounding line that is significantly more seaward than those determined by Bindschadler et al. (2011) and Scambos et al. (2007). So far, no other grounding line has been proposed over the area. In these static studies, GL is exclusively based on surface topographic features (basically the break in slope). If for large-scale glaciers or ice shelves the difference between this surface signature and the actual grounding line is rather limited compared to the size of the ice bodies (as can be seen from the comparison with ICEsat or InSAR data in Scambos et al. (2007) for instance), this difference can rapidly becomes of the order of the glacier typical size for smaller bodies like the Astrolabe Glacier where differences can locally reach 5 km. The automated procedures used for targeting surface topographic specific features (Bindschadler et al., 2011) or the large-scale filtering procedures sometimes corrupting upper surface topographic signatures (Scambos et al., 2007) lead to additional uncertainty. Close inspection of the SPIRIT DEM reveals that these two proposed grounding lines often cross areas where the surface exhibits a convex shape rather than the concave one expected in the vicinity of the break in slope (especially on the left flank of

TCD
7, 3969–4014, 2013

the glacier, see Fig. 4). Last, the ASAID and MOA grounding lines are inconsistent with the hydrostatic condition. The SPIRIT DEM gives an altitude of 130 m a.s.l. at the inland extremity of the QR radar profile (point R) which overlaps with the two grounding lines. Assuming floatation there, a simple hydrostatic calculation (with ρ_w and ρ_i respectively equal to 1028 kg m^{-3} and 890 kg m^{-3}) would give an ice thickness of 970 m which conflicts with that of 200 m inferred from the GPR survey (see Fig. 5).

For glaciers larger than the Astrolabe, the inconsistency between the two approaches used in the present study might become more pronounced. Indeed, larger ice thicknesses associated with larger tidal loading patterns will yield enhanced rigid deviations (G–F distances). Mapping the grounding line assuming hydrostatic equilibrium from both lower and upper ice surfaces measurements (which are nowadays widely available from airborne campaigns) remains reliable as long as the associated uncertainties are kept low. If bedrock slopes are steep as is the case with the Astrolabe, lateral shifts of the grounding line due to these errors are minimized. On the other hand, if the potentially more accurate kinematic approaches (GPS, satellite altimetric data...) have to be used, proper correction of the "elastic plate effect" is critical as the glacial system is large. In such a case, a 3-D elastic plate modelling allowing for spatially changing ice thicknesses should ideally be considered.

Acknowledgements. This study was funded by the **A**gence **N**ationale pour la **R**echerche (ANR) through the "DACOTA" project no. **ANR-06-VULN-016-01** and the "ADAGe" project no. **ANR-09-SYSC-001**. Field activities described here largely benifited from logistical and financial support from the French polar **I**nstitute **P**aul **E**mile **V**ictor (IPEV). E. Berthier acknowledges support from the French Space Agency (CNES) through the TOSCA and ISIS proposal #580. ICECAP operations over Astrolabe Glacier were funded by NASA's Ice Bridge program (**NNX09AR52G** and **NNX11AD33G** to the University of Texas at Austin); WISE was funded by a grant from NASA's IPY program to the Jet Propulsion Laboratory.

TCD
7, 3969–4014, 2013

The publication of this article
is financed by CNRS-INSU.

References

Bamber, J. and Bentley, C.: A comparison of satellite-altimetry and ice-thickness measurements of the Ross Ice Shelf, Antarctica, Ann. Glaciol., 20, 357–364, 1994. 3979

Bamber, J. L., Krabill, W., Raper, V., Dowdeswell, J. A., and Oerlemans, J.: Elevation changes measured on Svalbard glaciers and ice caps from airborne laser data, Ann. Glaciol., 42, 202–208, 2005.

Bindschadler, R., Choi, H., Wichlacz, A., Bingham, R., Bohlander, J., Brunt, K., Corr, H., Drews, R., Fricker, H., Hall, M., Hindmarsh, R., Kohler, J., Padman, L., Rack, W., Rotschky, G., Urbini, S., Vornberger, P., and Young, N.: Getting around Antarctica: new high-resolution mappings of the grounded and freely-floating boundaries of the Antarctic ice sheet created for the International Polar Year, The Cryosphere, 5, 569–588, doi:10.5194/tc-5-569-2011, 2011. 3975, 3981, 3990, 4000, 4003

Brotchie, J. F. and Silvester, R.: On crustal flexure, J. Geophys. Res., 74, 5240–5252, doi:10.1029/JB074i022p05240, 1969. 3986

Brunt, K. M., Fricker, H. A., Padman, L., Scambos, T. A., and O'Neel, S.: Mapping the grounding zone of the Ross Ice Shelf, Antarctica, using ICESat laser altimetry, Ann. Glaciol., 51, 71–79, doi:10.3189/172756410791392790, 2010. 3972, 3974, 3982, 3997

Corr, H. F. J., Doake, C. S. M., Jenkins, A., and Vaughan D. G.: Investigations of an "ice-plain" in the mouth of Pine Island Glacier, Antarctica, J. Glaciol., 47, 51–57, 2001. 3973

Craven, M., Carsey, F., Behar, A., Matthews, J., Brand, R., Elcheikh, A., Hall, S., and Treverrow, A.: Borehole imagery of meteoric and marine ice layers in the Amery Ice Shelf, East Antarctica, J. Glaciol., 51, 75–84, 2005. 3976, 3979

Durand, G., Gagliardini, O., Zwinger, T., Le Meur, E., and Hindmarsh, R.: Full Stokes modeling of marine ice sheets: influence of the grid size, Ann. Glaciol., 50, 109–114, 2009. 3971

TCD
7, 3969–4014, 2013

Fricker, H. A. and Padman, L.: Ice shelf grounding zone structure from ICESat laser altimetry, Geophys. Res. Lett., 33, L15502, doi:10.1029/2006GL026907, 2006. 3973, 3974
Fricker, H. A., Popov, S., Allison, I., and Young, N.: Distribution of marine ice beneath the Amery Ice Shelf, Geophys. Res. Lett, 28, 2241–2244, 2001. 3979
Gagliardini, O., Durand, G., Zwinger, T., Hindmarsh, R. C. A., and Meur, E. L.: Coupling of ice-shelf melting and buttressing is a key process in ice-sheets dynamics, Geophys. Res. Lett., 37, L14501, doi:10.1029/2010GL043334, 2010. 3972
Gudmundsson, G. H.: Ice-stream response to ocean tides and the form of the basal sliding law, The Cryosphere, 5, 259–270, doi:10.5194/tc-5-259-2011, 2011. 3985
Horgan, H. J. and Anandakrishnan, S.: Static grounding lines and dynamic ice streams: Evidence from the Siple Coast, West Antarctica, Geophys. Res. Lett., 33, L18502, doi:10.1029/2006GL27091, 2006. 3975
Joughin, I. and Padman, L.: Melting and freezing beneath Filchner-Ronne Ice Shelf, Antarctica, Geophys. Res. Lett., 30, 1477, doi:10.1029/2003GL016941, 2003. 3972
Joughin, I. R., Kwok, R., and Fahnestock, M. A.: Interferometric estimation of three-dimensional ice-flow using ascending and descending passes, IEEE T. Geosci. Remote, 36, 25–37, 1998. 3972
Joughin, I., Bamber, J. L., Scambos, T., Tulaczyk, S., Fahnestock, M., and MacAyeal, D. R.: Integrating satellite observations with modelling: basal shear stress of the Filcher-Ronne ice streams, Antarctica, Philos. T. R. Soc. A, 364, 1795–1814, 2006. 3974
Korona, J., Berthier, E., Bernard, M., Rémy, F., and Thouvenot, E.: SPIRIT. SPOT 5 stereoscopic survey of Polar Ice: Reference Images and Topographies during the fourth International Polar Year (2007–2009), ISPRS Journal of Photogrammetry and Remote Sensing, 2009. 3976, 4000
Legrésy, B., Wendt, A., Tabacco, I., Rémy, F., and Dietrich, R.: Influence of tides and tidal current on Mertz Glacier, Antarctica, J. Glaciol., 50, 427–435, doi:10.3189/172756504781829828, 2004. 3982
Le Meur, E.: Effects of a viscoelastic lithosphere on the isostatic bedrock response, Earth Planet. Sc. Lett., 188, 221–227, 2001. 3986
Pattyn, F., Huyghe, A., De Brabander, S., and De Smedt, B.: Role of transition zones in marine ice sheet dynamics, J. Geophys. Res.-Earth, 111, F02004, doi:10.1029/2005JF000394, 2006. 3971

TCD
7, 3969–4014, 2013

Rignot, E.: Hinge-line migration of Petermann Gletscher, north Greenland, detected using satellite radar interferometry, J. Glaciol., 44, 469–476, 1998. 3974
Rignot, E. and Jacobs, S. S.: Rapid bottom melting widespread near Antarctic ice sheet grounding lines, Science, 296, 2020–2023, 2002. 3972
Rignot, E., Mouginot, J., and Scheuchl, B.: Antarctic grounding line mapping from differential satellite radar interferometry, Geophys. Res. Lett., 38, L10504, doi:10.1029/2011GL47109, 2011. 3972, 3973, 3974, 3975, 3983
Robin, G.,Doake, C. S. M., Kohnen, H., Crabtree, R. D., Jordan, S. R., and Moller, D.: Regime of the Filchner-Ronne ice shelves, Antarctica, Nature, 302, 582–586, 1983. 3973
Scambos, T. A., Haran, T. M., Fahnestock, M. A., Painter, T. H., and Bohlander, J.: MODIS-basedh Mosaic of Antarctica (MOA) data sets: Continent-wide surface morphology and snow grain size, Remote Sens. Environ., 111, 242–257, 2007. 3974, 3981, 3990, 4000, 4003
Schoof, C.: Ice sheet grounding line dynamics: Steady states, stability, and hysteresis, J. Geophys. Res.-Earth, 112, doi:10.1029/2006JF000664, 2007. 3971
Shepherd, A. et al.: A Reconciled Estimate of Ice-Sheet Mass Balance, Science, 338, 1183–1189, 2012. 3972
Shuman, C. A., Berthier, E., and Scambos, T. A.: 2001–2009 elevation and mass losses in the Larsen A and B embayments, Antarctic Peninsula, J. Glaciol., 57, 737–754, 2011.
Van der Veen, C. J.: Fracture mechanics approach to penetration of surface crevasses on glaciers, Cold Reg. Sci. Technol., 27, 31–47, 1998. 3978
Vaughan, D.: Tidal flexure at ice shelf margins, J. Geophys. Res, 100, 6213–6224, 1995. 3973, 3982, 3983, 3986
Vaughan, D. G., Corr, H. F. J., Bindschadler, R. A., Dutrieux, P., Gudmundsson, G. H., Jenkins, A., Newman, T., Vornberger, P., and Wingham, D. J.: Subglacial melt channels and fracture in the floating part of Pine Island Glacier, Antarctica, J. Geophys. Res., 117, doi:10.1029/2012JF002360, 2012. 3978
Wen, J., Jezek, K. C., Csathó, B. M., Herzfeld, U. C., Farness, K. L., and Huybrechts, P.: Mass budgets of the Lambert, Mellor and Fisher Glaciers and basal fluxes beneath their flowbands on Amery Ice Shelf, Sci. China Ser. D, 50, 1693–1706, 2007. 3979
Wen, J., Wang, Y., Wang, W., Jezek, K. C., Liu, H., and Allison, I.: Basal melting and freezing under the Amery Ice Shelf, East Antarctica, J. Glaciol., 56, 81–90, 2010. 3979
Young, D. A., Wright, A. P., Roberts, J. L., Warner, R. C., Young, N. W., Greenbaum, J. S., Schroeder, D. M., Holt, J. W., Sugden, D. E., Blankenship, D. D., van Ommen, T. D., and

TCD
7, 3969–4014, 2013

Siegert, M. J.: A dynamic early East Antarctic Ice Sheet suggested by ice covered fjord landscapes, Nature, 474, 72–75, doi:10.1038/nature10114, 2011. 3980

Zwally, H. J., Giovinetto, M. B., Li, J., Cornejo, H. G., Beckley, M. A., Brenner, A. C., Saba, J. L., and Yi, D.: Mass changes of the Greenland and Antarctic ice sheets and shelves and contributions to sea-level rise: 1992–2002, J. Glaciol., 51, 509–527, 2005. 3976

TCD

7, 3969–4014, 2013

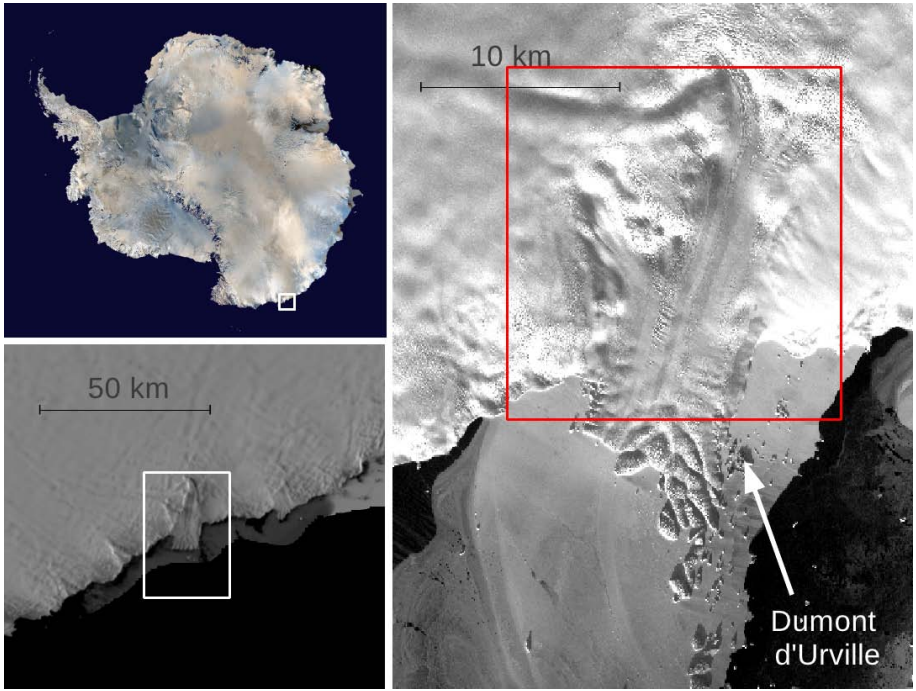

Fig. 1. Location of the Astrolabe Glacier in the Terre Adelie sector of East Antarctica from a MOA(MODIS) global picture (left) and a SPOT close up on the right (©CNES/Distribution Spot Image). The red square shows the location of Fig. 4.

TCD
7, 3969–4014, 2013

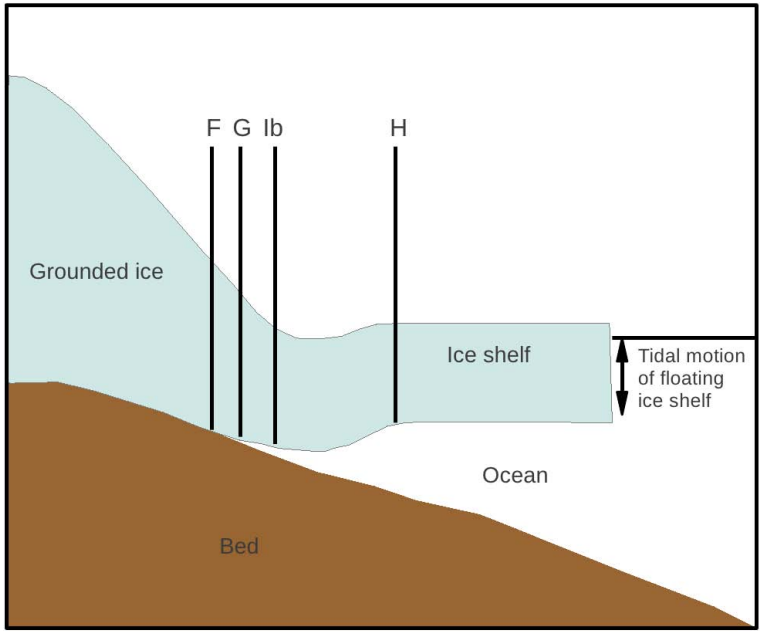

Fig. 2. Important points along the transition between grounded and floating ice. F represents the landward limit of tidally-induced vertical displacements, G the grounding line where the ice bottom actually splits from the ground, Ib the so called “break in slope” and H the limit where the rigid effects of the elastic bending of the ice slab do not propagate, allowing the ice to freely float on the ocean, (adapted from Brunt et al. (2010)).

TCD
7, 3969–4014, 2013

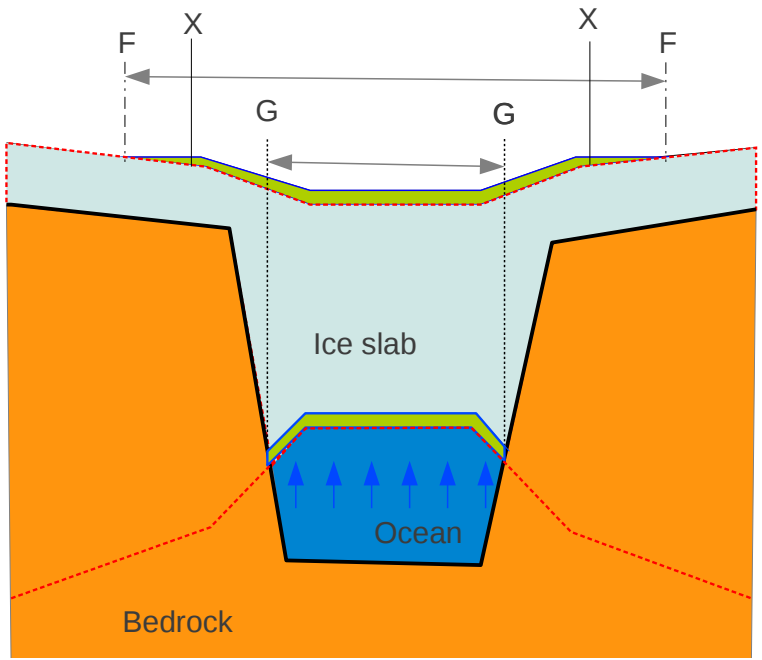

Fig. 3. Sketch of the ice slab/ocean interactions. Red upper and lower dotted lines correspond to the hydrostatic long term equilibrium positions of respectively the upper ice surface and the corresponding theoretical floatation depths. Points where these latter depths cross the bedrock topography determine the GL points considered as a good approximation of the grounding line. The ocean push and the corresponding elastic rigid flexure of the ice upper surface are featured by the green strips. Points labelled X (later referred to as "control points") represent what the GPS method of Sect. 6 could give once the upper surface displacements become significant. Last, F represents the landward limit of these upper surface displacements.

TCD
7, 3969–4014, 2013

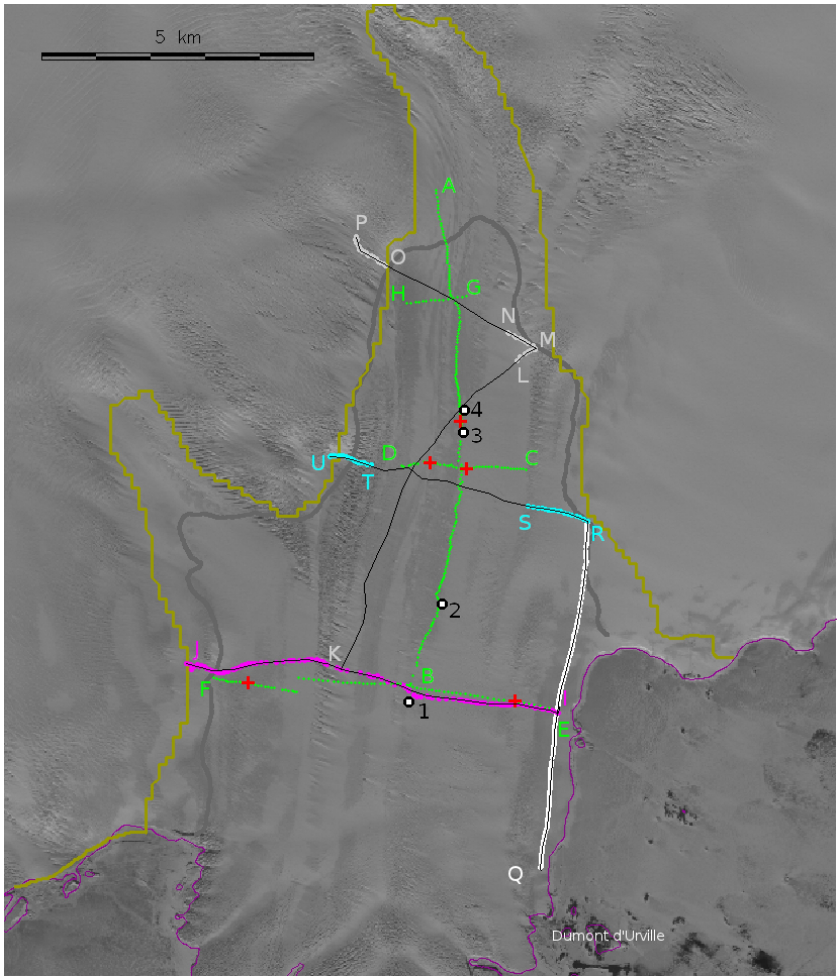

Fig. 4. (Caption on next page.).

TCD
7, 3969–4014, 2013

Fig. 4. Summary map of field activities deployed from the ground carried out on the Astrolabe Glacier superimposed on a SPOT-HRS image (Korona et al. (2009), ©CNES 2007/Distribution Spot Image). The thin black line outlines the ground radar profiles actually measured and the overlapping coloured dots the points where the ice bottom echo was detectable allowing for a depth to be inferred. Green dots represent each of the points measured twice by kinematic GPS in order to constitute the profiles of difference in ice surface elevation and red crosses the resulting "GPS control points" (see Sect. 6). Points 1 to 4 are the drop-off spots where surface elevation was continuously monitored by GPS (Sect. 4.2.2). Last, the gray and brown continuous curves are the grounding lines proposed by respectively Bindschadler et al. (2011) and Scambos et al. (2007).

TCD
7, 3969–4014, 2013

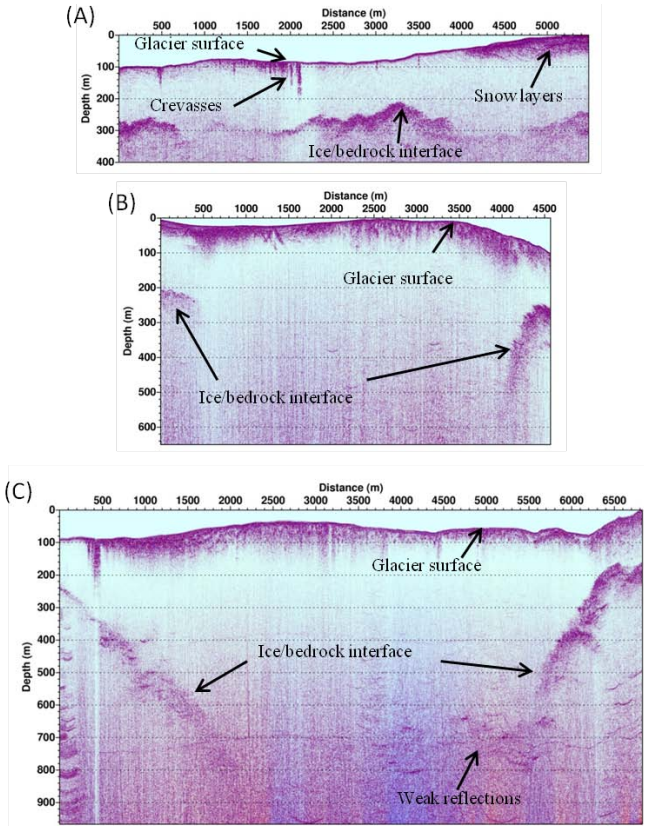

Fig. 5. Ice-bedrock interface measured by GPR along profiles QR **(A)**, RU **(B)**, and IJ **(C)** of Fig. 4. Snow layers horizons become visible on the QR profile after a distance of 4000 m when entering the accumulation zone. Combined effects of depth and floating ice seriously alter the reflectors in the middle of the IJ profile and lead to a total loss in the middle of the RU profile.

TCD
7, 3969–4014, 2013

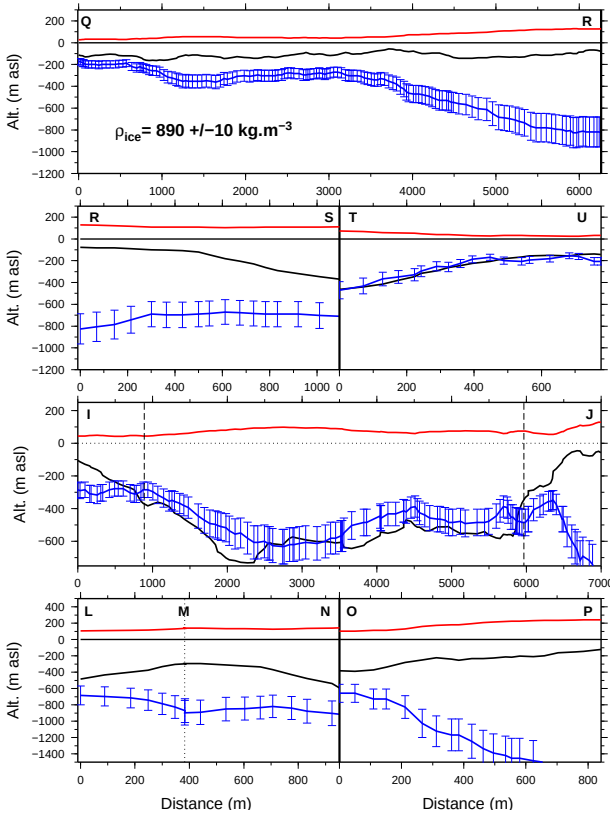

Fig. 6. Theoretical hydrostatic floatation depth (blue curve with error bars) computed with an ice density of $890 \pm 10\,\mathrm{kg\,m^{-3}}$ compared to the ice bottom depth (black curve) inferred from Ground Penetrating Radar. The red curve represents the geoidal altitude of the ice upper surface obtained from the SPIRIT DEM. The profiles correspond to the coloured dots on Fig. 4. The vertical dashed lines on profile IJ show the location of to the 2 control points for the grounding line position obtained from the GPS kinematic method, (see Sect. 6).

TCD
7, 3969–4014, 2013

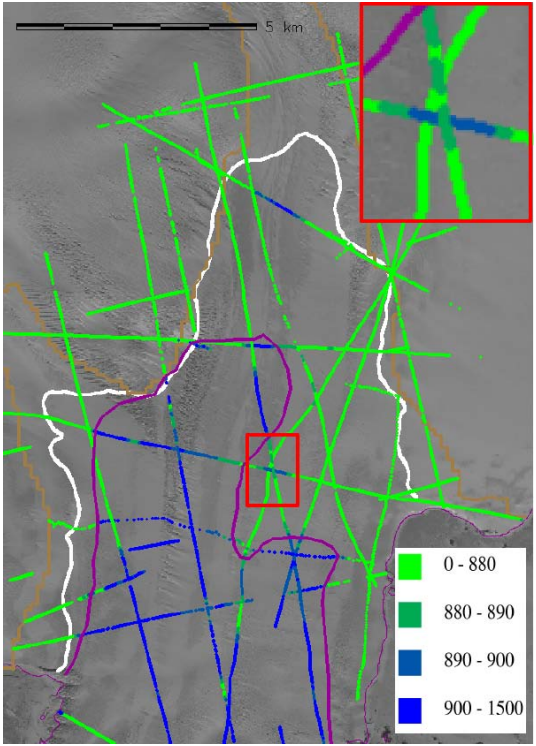

Fig. 7. Hydrostatically determined transitions between grounded (green) and floating (blue) ice along all radar profiles performed over the coastal part of the Astrolabe Glacier as a function of the chosen value for ice density. Assuming the central value of 890 kg m^{-3} for the ice density and giving more credit to the ground radar profiles when conflicting with airborne ones (see text), a grounding line position is proposed under the form of the purple line. The inset allows to visualize the detail of the different color transitions according to the chosen ice density. The white and brown continuous lines are the grounding lines as proposed by Bindschadler et al. (2011) and Scambos et al. (2007).

TCD
7, 3969–4014, 2013

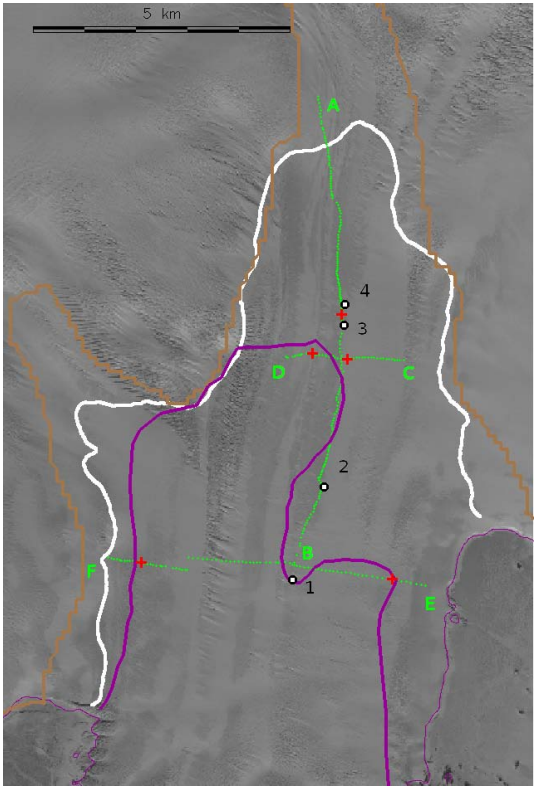

Fig. 8. Profiles made of measurement points (green dots) at which difference in ice upper altitude between high and low tides has been measured by GPS. Also featured is the grounding line preceding estimation. Red crosses represent the transition points where this difference becomes significant (see text in Sect. 4.2.1) and points 1 to 4 the points where GPS have been dropped and have recorded continuously (Sect. 4.2.2).

TCD
7, 3969–4014, 2013

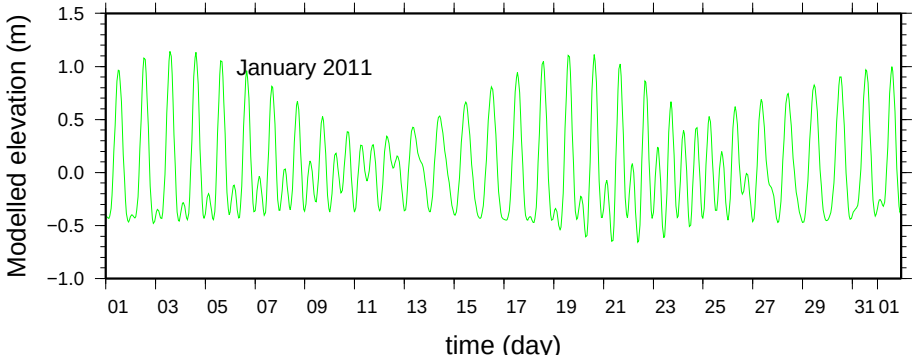

Fig. 9. Modelled tides for January 2011 where semi-dirurnal, diurnal and fortnighlty tidal periods are observable.

TCD
7, 3969–4014, 2013

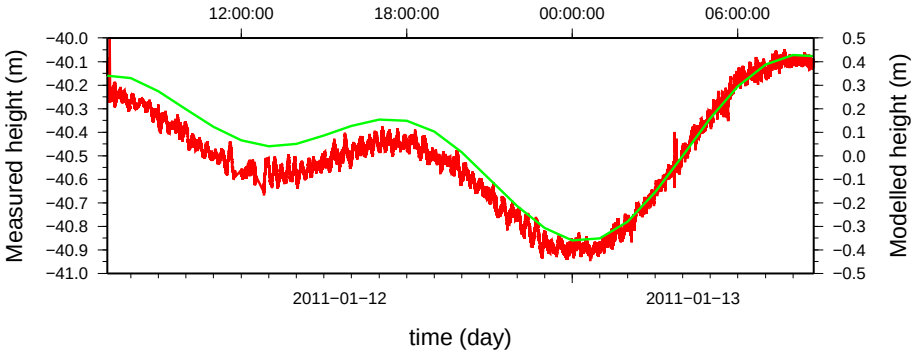

Fig. 10. Modelled (green) and measured (red) tides between the 12 and 13 January 2011. Surface displacements were measured by differential GPS with a baseline of less than 400 m allowing for very accurate measurements and a noise level of less than 5 cm.

TCD
7, 3969–4014, 2013

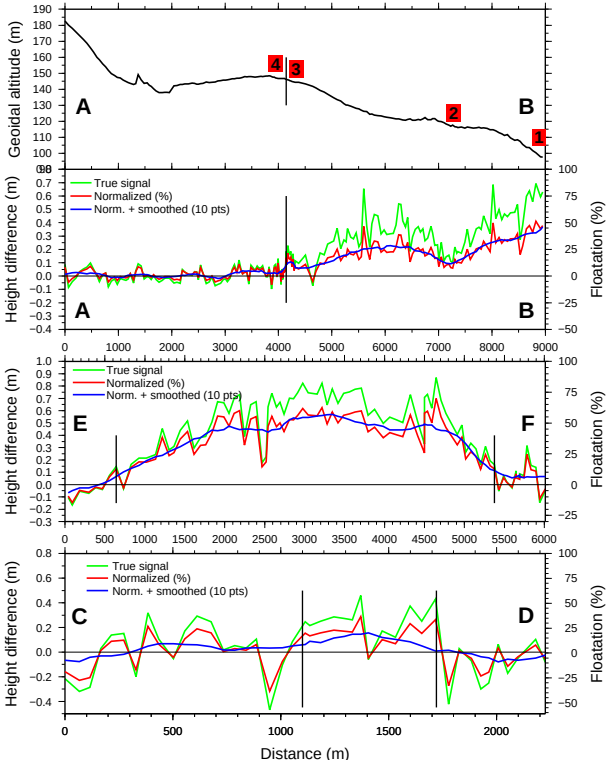

Fig. 11. Difference in ice surface altitude between high and low tide for profile [AB], [EF] and [CD]. The green curve represent true GPS data difference, whereas the red one represents this difference scaled to the tidal amplitude (expressed in percentage). The blue line is a smoothing (over 10 points) of the red curve. Locations where the altitude difference becomes significant are featured by the black vertical line and define our grounding line control points. The altitude above sea level for profile [AB] is also displayed on top along with the positions of the 4 drop off points along the profile (see Sect. 4.2.2).

TCD
7, 3969–4014, 2013

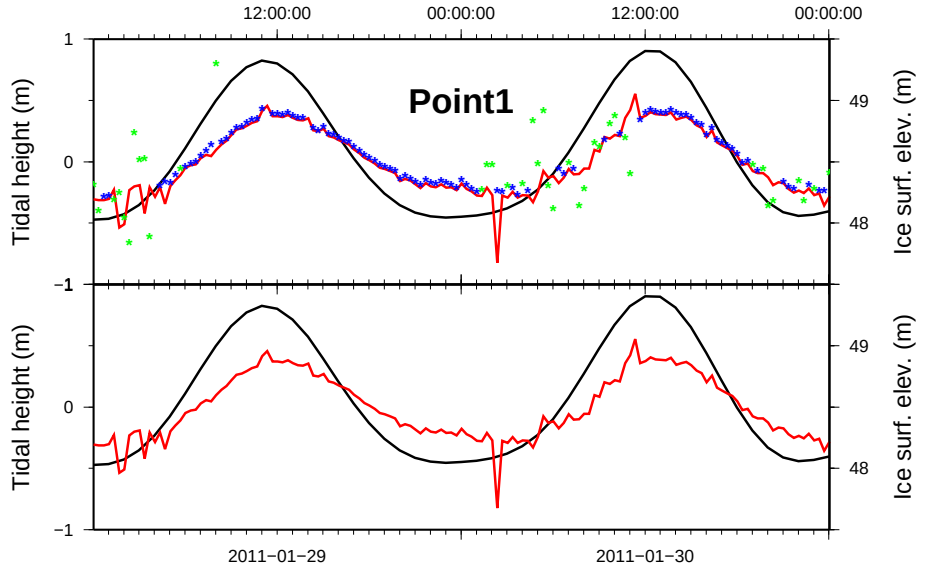

Fig. 12. Time-dependant surface displacements during 2 days in january 2011 at Point 1. On the bottom panel are shown the tidal signal (black) compared to the vertical ice upper surface displacements obtained in RTK differential mode (red). GPS data were also post-processed so as to confirm the validity of the RTK method. Corresponding results are depicted as blue stars (upper panel) when ambiguities where fixed and as green stars otherwise. The consistency between the red curve and the set of blue dots confirms the validity of the RTK approach whose results are then later systematically used in Fig. 13.

TCD
7, 3969–4014, 2013

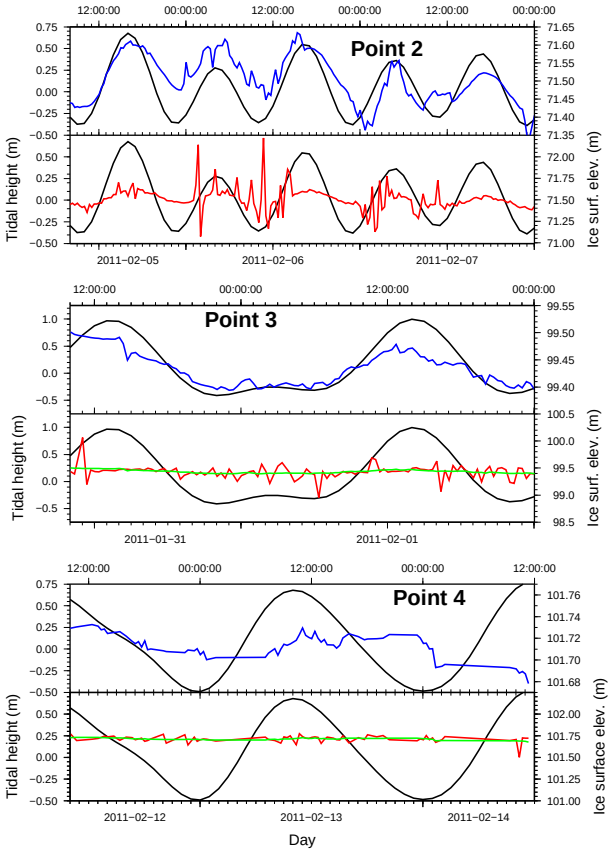

Fig. 13. Comparison of the upper surface displacements and tides for Point 2, 3 and 4. Black curves represent the tidal amplitude whereas the red ones stand for raw RTK GPS positions. Blue curves result from a 10-point smoothing of the raw data to which a vertical amplification has been applied (varying according to the point) in order to confirm or deny any correlation with the tides. Green curves for points 3 and 4 just represent the smoothing of raw GPS data.

TCD
7, 3969–4014, 2013

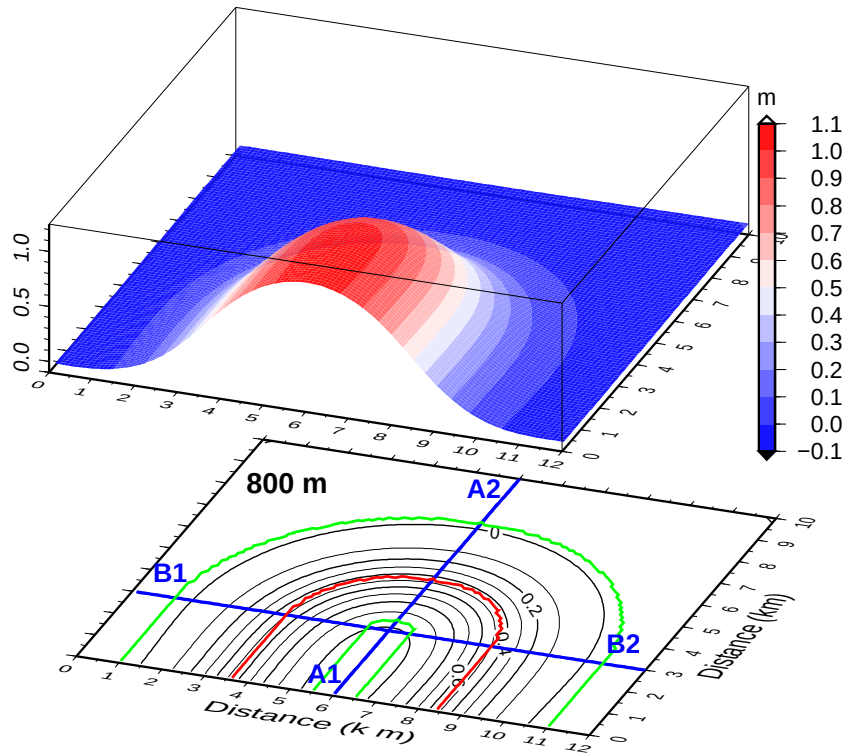

Fig. 14. Elastic bulging of a 800 m thick ice slab (upper part) in reponse to a 1 m bottom water push exerted over the domain as outlined in red (bottom part). Green contours show the two extreme fjord geometries of the sensitivity test (see Fig. 16) whereas the black ones are the deformation contours corresponding to the 3-D upper view. Aslo outlined are the two cross sections represented in Fig. 15.

TCD
7, 3969–4014, 2013

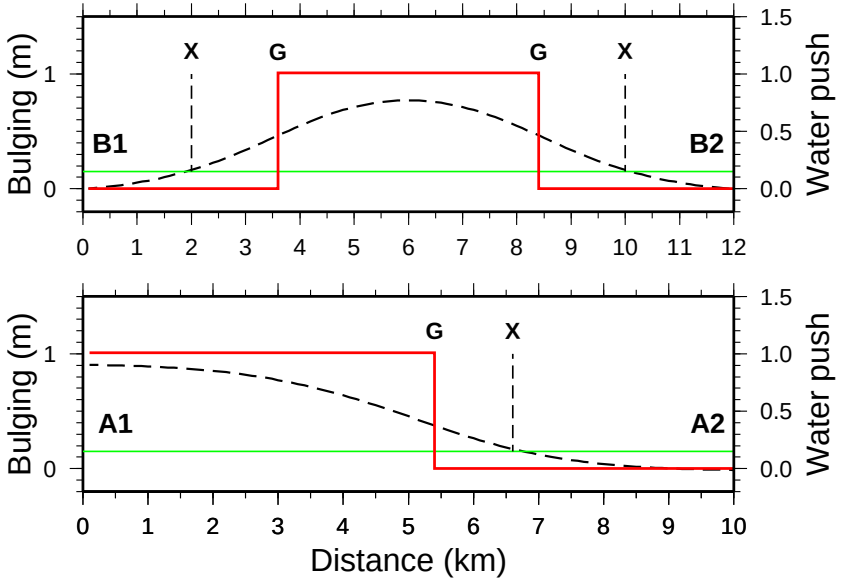

Fig. 15. Longitudinal and orthogonal cross sections of both the loading pattern (red) and corresponding ice surface uplift (black) along profiles A1–A2 and B1–B2 of Fig. 14. The green horizontal line represents the surface smallest displacement of 0.15 m detectable by the kinematic GPS measurements. Full floatation expressing hydrostatic equilibrium implies a 1 m uplift as is almost the case on the left part of the A1–A2 profile (mouth of the fjord). The water push is here expressed as the weight exerted over each cell of the domain ($100 \times 100 \times \rho_w g \delta$) in 10^8 kg.

TCD
7, 3969–4014, 2013

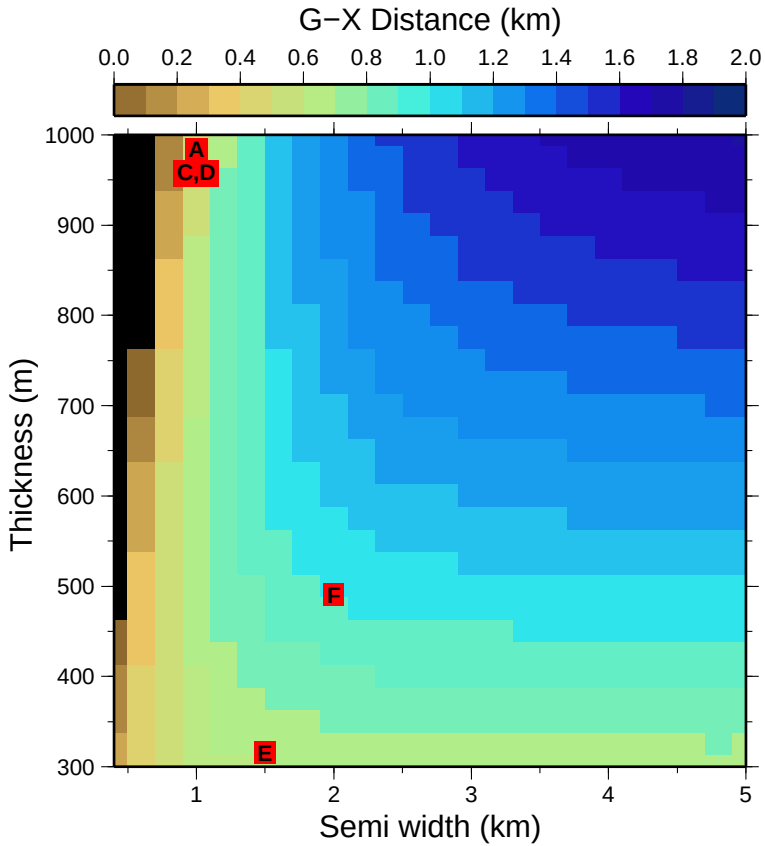

Fig. 16. G-X distance (km) as a function of the ice slab thickness and the semi width of the forcing pattern. The five kinematic GPS control points A, C, D, E and F are here placed according to their specific parameter combinations. For display purpose, point A (1050 m ice thickness) had to be lowered to 975 m.

TCD
7, 3969–4014, 2013

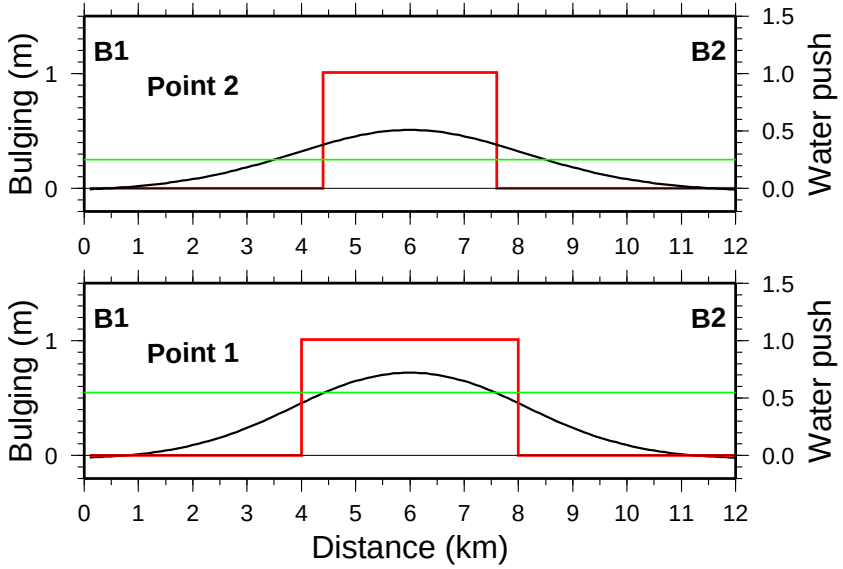

Fig. 17. Profiles of ice upper deformation and oceanic forcing for drop-off Points 1 and 2 whose respective ice thickness/load semi-width combinations are 700 m/2 km and 850 m/1.6 km. The green horizontal line corresponds to floatation percentages of 55 % and 25 % for points 1 and 2.

TCD
7, 3969–4014, 2013

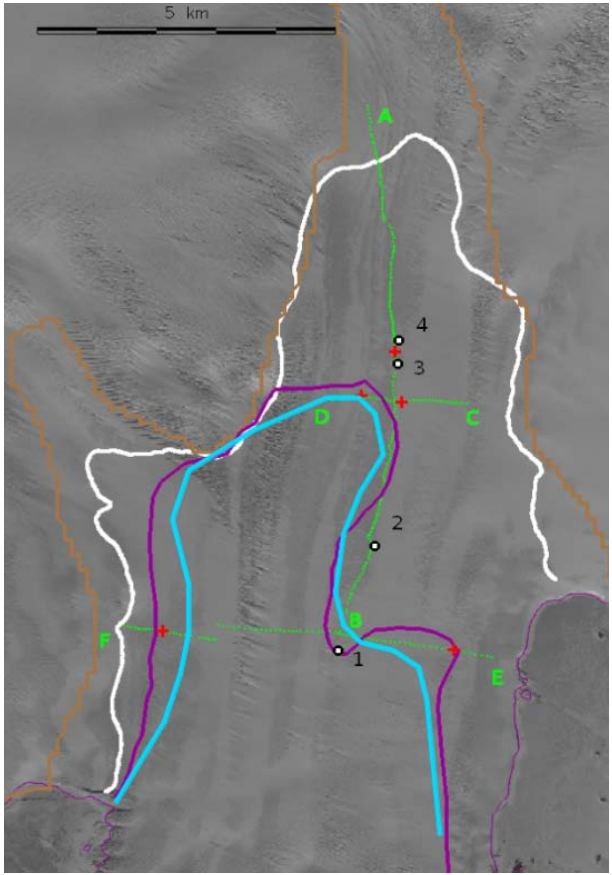

Fig. 18. Updated grounding line position (blue curve) from static radar and GPS kinematic data.

TCD
7, 3969–4014, 2013